



HAL
open science

On the Calibration of Cohesive Parameters for Refractories from Notch Opening Displacements in Wedge Splitting Tests

R Vargas, R B Canto, François Hild

► **To cite this version:**

R Vargas, R B Canto, François Hild. On the Calibration of Cohesive Parameters for Refractories from Notch Opening Displacements in Wedge Splitting Tests. *Journal of the European Ceramic Society*, 2021, 41 (14), pp.7348-7361. 10.1016/j.jeurceramsoc.2021.07.011 . hal-03282215

HAL Id: hal-03282215

<https://hal.science/hal-03282215v1>

Submitted on 8 Jul 2021

HAL is a multi-disciplinary open access archive for the deposit and dissemination of scientific research documents, whether they are published or not. The documents may come from teaching and research institutions in France or abroad, or from public or private research centers.

L'archive ouverte pluridisciplinaire **HAL**, est destinée au dépôt et à la diffusion de documents scientifiques de niveau recherche, publiés ou non, émanant des établissements d'enseignement et de recherche français ou étrangers, des laboratoires publics ou privés.

On the Calibration of Cohesive Parameters for Refractories from Notch Opening Displacements in Wedge Splitting Tests

R. Vargas^{a,c}, R.B. Canto^{a,b} and F. Hild^c

^aFederal University of São Carlos, Graduate Program in Materials Science and Engineering (PPGCEM), 13565-905, São Carlos-SP, Brazil

^bFederal University of São Carlos (UFSCar), Department of Materials Engineering (DEMa), 13565-905, São Carlos-SP, Brazil, Brazil

^cUniversité Paris-Saclay, ENS Paris-Saclay, CNRS, LMT - Laboratoire de Mécanique et Technologie, 91190 Gif-sur-Yvette, France

ARTICLE INFO

Keywords:

Cohesive Zone Model (CZM)

Digital Image correlation (DIC)

Finite Element Model Updating (FEMU)

Notch Opening Displacement (NOD)

Refractory castable

Wedge Splitting Test (WST)

ABSTRACT

Cohesive elements are commonly used to describe crack propagation in heterogeneous materials with toughening mechanisms. This work aims to provide a guideline on how these fracture parameters can be calibrated using notch opening displacements (NOD) measured via digital image correlation and force data from wedge splitting tests (WSTs). Weighted finite element model updating was applied to calibrate material and boundary condition parameters in the same framework. The influence of each parameter on force and NOD data are given together with uncertainties for the calibrated parameters. Numerical results showed very good agreement in terms of splitting force, NOD, displacement and gray level residual fields. It is shown that images obtained during WSTs focusing on the crack path (*i.e.*, hiding the loading region) can be used to drive numerical simulations and obtain cohesive parameters.

*Corresponding author

 r.vargas_m@ppgcem.ufscar.br (R. Vargas)

ORCID(s): 0000-0002-1711-9804 (R. Vargas); 0000-0002-9286-9912 (R.B. Canto); 0000-0001-5553-0066 (F. Hild)

1. Introduction

Refractories are known to maintain functional properties in very hazardous conditions such as high-temperature and corrosive environments [1, 2]. Therefore, understanding their fracture mechanisms and modeling their development is of utmost importance to optimize processes and minimize risks [3]. In such severe in-service conditions, crack initiation is unavoidable [4] and thus it is usual practice to limit propagation via toughening mechanisms [5, 6]. The latter ones lead to the formation of fracture process zones (FPZs) where cracks have some cohesion between the newly created surfaces. Linear elastic fracture mechanics (LEFM) was applied for structures with very small defects made of brittle materials, although severe deviations may arise in the presence of a developed FPZ, especially in small specimens [7]. Therefore, this work focuses on cohesive zone models (CZMs) suitable to be calibrated under usual laboratory characterization of materials, aiming to provide first estimates of parameters needed prior to simulating in-service applications.

The use of traction-separation laws to describe the FPZ [8, 9, 10] has been successfully applied to refractory materials with different approaches. For instance, CZMs were used to study thermal shocks [11] and to check size effects and deviations from LEFM [7]. Later on, they were utilized for analyzing damage during thermal cycles [12] and fracture [13] in various refractories. The same models may also be used to study interface cohesion in such heterogeneous materials [14, 15, 16]. More recently, several examples are found about its usage to simulate initiation and propagation of macrocracks [17, 18, 19, 20, 21, 22].

In few of the afore-cited references, the material parameters were estimated without experimental exploration [7, 16]. Some of them briefly comment on parameter calibration without giving many details [12, 13, 14]. For the quantity to be optimized with respect to experimental information, the crack mouth opening displacement (CMOD) [11, 17] or elastic properties obtained from acoustic measurements [15, 17] can be used. More recently, inverse algorithms were used to find the best fit of the loading curve [18, 19]. Vargas et al. [20] used measured CMODs to prescribe boundary conditions and used the force measurements in the cost function of a Finite Element Model Updating (FEMU) procedure, while Doitrand et al. [21] also used force measurement and crack lengths estimates to find the best fit through manual optimization.

Jiménez-Piqué et al. [13] mentioned the use of digital image correlation (DIC) in the calibration procedure of a Hillerborg et al. [23] model. DIC was applied to estimate the “transition from microcracking to bridging and the approximate contribution of both mechanisms.” More recently, CMODs measured by DIC were applied as boundary conditions for the calibration of CZM parameters [20, 22]. The authors also calculated displacement residuals between experimental and numerical results, as well as gray level residuals directly in the images using the kinematics from the Finite Element (FE) simulation. Doitrand et al. [21] considered strain fields assessed via DIC to look for crack branches on the surface, to estimate the crack length using a user-defined threshold, and to define a tortuous crack path

with cohesive elements. The authors also tested a set of different parameters to check which one would best fit the experimental force and crack lengths.

In a previous work, room temperature and 600°C Wedge Splitting Tests (WSTs) [24, 25] were performed to analyze how fracture parameters changed under these conditions for samples with different sintering temperatures [26]. However, the window size of the furnace limited the field of view hiding the force application region. This difficulty led to the study of the relationship between notch opening displacements (NODs) and CMODs [22]. In the present work, the NOD extrapolation to CMOD proposed in Ref. [22] is used to drive numerical simulations. The corresponding parameters are calibrated together with material parameters in a specially tailored identification procedure. First, the identification framework is introduced. Then, one benchmark experiment is tested to validate the proposed methodology before applying it to the room temperature experiment in which the CMOD was not accessible.

2. Calibration of CZM parameters

This work proposes to calibrate CZM parameters using NOD data to drive FE simulations. The so-called Finite Element Model Updating (or FEMU [27, 28, 29]) framework is first introduced. Then, the geometry, boundary conditions, and all the necessary parameters for the methodology are described.

2.1. Identification strategy

The FEMU method is used hereafter. The identification technique, which is based on a Gauss-Newton scheme, consists in nonlinear least squares minimization of χ^2 with respect to n_p parameters gathered in the column vector $\{\mathbf{p}\}$

$$\chi^2(\{\mathbf{p}\}) = \omega_F \chi_F^2(\{\mathbf{p}\}) + \omega_{\text{NOD}} \chi_{\text{NOD}}^2(\{\mathbf{p}\}) \quad (1)$$

where χ_F^2 denotes the cost function for global equilibrium

$$\chi_F^2(\{\mathbf{p}\}) = \frac{1}{n_t} \sum_t \left(\frac{F_m(t) - F_{\text{FE}}(t, \{\mathbf{p}\})}{\sigma_F} \right)^2 \quad (2)$$

and χ_{NOD}^2 that related to the Notch Opening Displacement (NOD)

$$\chi_{\text{NOD}}^2(\{\mathbf{p}\}) = \frac{1}{n_t} \sum_t \left(\frac{\text{NOD}_m(t) - \text{NOD}_{\text{FE}}(t, \{\mathbf{p}\})}{\sigma_{\text{NOD}}} \right)^2 \quad (3)$$

in which the subscript m is related to the measured quantities (*i.e.*, force and NOD from load cell and DIC, respectively) and FE to computed quantities in FE analyses, n_t the number of time steps, σ_F and σ_{NOD} the standard measurement uncertainties, for force and NOD, respectively. Both weights (ω_F and ω_{NOD}) in the total cost function are equal via Bayesian statistics [30]

$$\omega_F = \frac{1}{2} \quad \text{and} \quad \omega_{\text{NOD}} = \frac{1}{2} \quad (4)$$

since the number of considered data is identical in each individual cost function. In such framework, χ_F and χ_{NOD} are direct estimates of model quality since the closer they are to unity, the higher the probability that experimental noise be the source of error and not the chosen model.

The sensitivities for both F_{FE} and NOD_{FE} with respect to the sought parameters $\{\mathbf{p}\}$ are rectangular $n_t \times n_p$ matrices $[\mathbf{S}_F]$ and $[\mathbf{S}_{\text{NOD}}]$

$$[\mathbf{S}_F] = \left[\frac{\partial F_{\text{FE}}}{\partial \{\mathbf{p}\}}(t, \{\mathbf{p}_n\}) \right] \quad \text{and} \quad [\mathbf{S}_{\text{NOD}}] = \left[\frac{\partial \text{NOD}_{\text{FE}}}{\partial \{\mathbf{p}\}}(t, \{\mathbf{p}_n\}) \right] \quad (5)$$

calculated by finite differences with a perturbation of 1% of each parameter with respect to the current estimates. After linearization of F_{FE} and NOD_{FE} with respect to the parameter corrections $\{\delta\mathbf{p}\}$, the minimization procedure consists in iteratively updating the current estimates $\{\mathbf{p}_n\}$ of the parameter vector by solving linear systems

$$[\mathbf{H}] \cdot \{\delta\mathbf{p}\} = \{\mathbf{h}\} \quad (6)$$

where $[\mathbf{H}]$ is the dimensionless Hessian

$$[\mathbf{H}] = \frac{1}{\sigma_F^2} [\mathbf{S}_F]^\top [\mathbf{S}_F] + \frac{1}{\sigma_{\text{NOD}}^2} [\mathbf{S}_{\text{NOD}}]^\top [\mathbf{S}_{\text{NOD}}] \quad (7)$$

and $\{\mathbf{h}\}$ the right hand member

$$\{\mathbf{h}\} = \frac{1}{\sigma_F^2} [\mathbf{S}_F]^\top \{F_m(t) - F_c(t, \{\mathbf{p}_n\})\} + \frac{1}{\sigma_{\text{NOD}}^2} [\mathbf{S}_{\text{NOD}}]^\top \{\text{NOD}_m(t) - \text{NOD}_{\text{FE}}(t, \{\mathbf{p}_n\})\} \quad (8)$$

Convergence is deemed successful when the root mean square (RMS) of the relative variation of the parameters is less than 10^{-2} between two subsequent iterations.

The sensitivity matrices, and more importantly their condensed effect described by the Hessian matrix, give access to the covariance matrix $[\mathbf{C}]$ of the calibrated parameters

$$[\mathbf{C}] = [\mathbf{H}]^{-1} \quad (9)$$

in which the square root of each diagonal term expresses a fraction related to the standard deviation for each parameter when considered alone. The latter will be reported in the following results.

2.2. Parameters in the identification framework

The different regions considered herein are shown in Figure 1 in the reference images of the two analyzed tests. The sample geometry that was used in the FEMU procedure corresponds to red contours, and the two nodes where displacement boundary conditions (BCs) were applied are highlighted in blue circles. The CMOD (extrapolated from NOD data) was used to drive FE simulations applying half of the opening for the horizontal component on each side. Zero amplitudes were prescribed for the vertical component of these two points. The NODs were measured in the yellow squares and the cyan polygons depict the region where conventional DIC was performed.

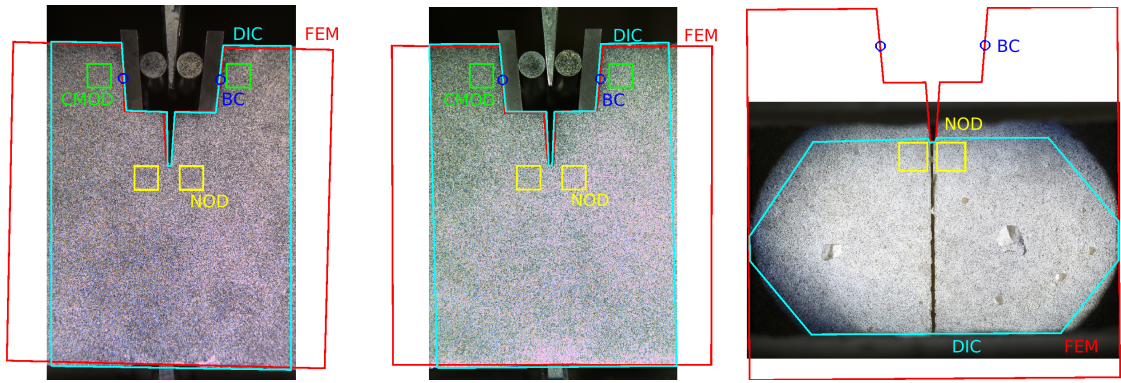


Figure 1: Sample geometry in the reference images for the benchmark case ((a) front and (b) back surfaces) and WST-MZ1-S1450G (c). The geometry used for the FE procedure is depicted in red (100 mm in height and width, and 72.5 mm (a,b) or 75 mm (c) in thickness), and the regions where Dirichlet boundary conditions were applied in blue circles. NODs were measured in the yellow squares, and the displacements were compared to DIC results in the cyan region.

For the FE simulations, the PPR cohesive law [31, 32] was chosen. The shape parameter α and the initial slope λ were equal to 7 and 0.005, as chosen for the same material investigated in Ref. [20]. It was assumed that the cohesive strength σ_f was identical for modes I and II, and the fracture energy J_c for modes I and II was also the same since in this quasi pure mode I test no sensitivity was expected to uncouple the parameters for each mode in the identification procedure [33]. The traction-separation laws for the initial CZM parameters are shown in Figure 2. It is worth noting that only the cohesive strength σ_f and the fracture energy J_c (integral of the traction-separation curve) were calibrated hereafter.

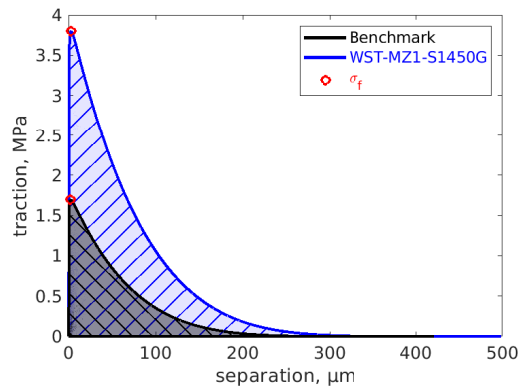


Figure 2: PPR traction-separation law using the initial parameters (see Table 1). The cohesive strength σ_f corresponds to the maximum traction (red circles), and the fracture energy J_c is the integral of the traction-separation curve (dashed areas).

The calibration procedure was first tested in a benchmark case (Figure 1(a-b)) in which CMOD data were available as well as images from both sides of the WST specimen. The material for this experiment was fired at 540°C and

was made using the DD40 grade made by IBAR-Brazil (*i.e.*, an anti-erosive commercial refractory castable designed for petrochemical applications [34, 35, 36]). This refractory contains quartz, mullite, kyanite, β -cristoballite and alumina [35]. Then, the so-called WST-MZ1-S1450G experiment (Figure 1(c)) was studied where only NOD data were available. The nomenclature is after the designation MZ1-S1450G used in Refs. [26, 22], namely, the sample was made of alumina with mullite-zirconia aggregates (MZ), fired at 1450°C (S1450), and lateral grooves (G) were implemented to guide propagation crack. This material was also produced by IBAR-Brazil.

Although an earlier identification was performed using only force data for the benchmark case, the initial parameters were chosen from another experiment performed on the same material [22] for comparison purposes, and to initialize the FEMU procedure farther away from a possibly optimal solution. For WST-MZ1-S1450G, σ_f was initially set from the value obtained in Ref. [20] (*i.e.*, another material with similar geometry) multiplied by the ratio between the ultimate load in both experiments. The initial fracture energy J_c was assumed as twice that measured from the loading curve of this experiment [26].

Since the CMOD region (close to the blue circles in Figure 1) was not accessible in WST-MZ1-S1450G (Figure 1(c)), the extrapolation proposed in Ref. [22] was used hereafter. This proposal is based on the distinction of the NOD (δ) vs. CMOD (Δ) relationship into two regimes, namely, a quadratic interpolation for the pre-peak regime

$$\frac{\delta}{\delta(F_{max})} = \left(\frac{\Delta(F_{max})}{c\delta(F_{max})} - 1 \right) \left(\frac{\Delta}{\Delta(F_{max})} \right)^2 + \left(2 - \frac{\Delta(F_{max})}{c\delta(F_{max})} \right) \frac{\Delta}{\Delta(F_{max})} \quad (10)$$

and an affine trend for the post-peak regime

$$\frac{\delta - \delta(F_{max})}{\delta(F_{max})} = \frac{\Delta(F_{max})}{c\delta(F_{max})} \left(\frac{\Delta - \Delta(F_{max})}{\Delta(F_{max})} \right) \quad (11)$$

where c is the slope of the latter Δ vs. δ interpolation. In the proposed framework, both portions are made C^1 (*i.e.*, continuous first order derivative) at the peak load ($F = F_{max}$). Therefore, two parameters are needed to calculate Δ from δ data, namely, $\Delta(F_{max})$ and c , since $\delta(F_{max})$ is experimentally measured. Both of these parameters are then added to the list of parameters so that Equations (10) and (11) provide the boundary conditions to the whole simulation. The NOD δ was measured by DIC and both parameters were initialized in the iterative procedure with those of the cyclic case reported in Ref. [22]. For easier implementation, instead of identifying $\Delta(F_{max})$, this parameter is substituted by the ratio $R = \Delta(F_{max})/\delta(F_{max})$.

Two more parameters were introduced in the identification scheme. The so-called Boundary Condition correction is defined by

$$\Delta_{BCc} = (BCc - 1) \times \Delta(F_{50\%}) \quad (12)$$

in which $\Delta(F_{50\%})$ is the CMOD at 50% of the ultimate load (pre-peak) and Δ_{BCc} consists in a correction for a non-zero force in the reference state and also corrects the kinematics of some possible wedge misalignment [20]. Δ_{BCc}

is defined as a scalar and is interpreted as the percentage of the NOD from the time step where the force was 50% of the ultimate load. This parameter is taken as unity in the first iteration since it would be the case if no correction were needed.

Last, the Young's modulus is the sixth parameter, and its first estimate comes from an independent evaluation through impulse excitation technique. All the initial parameters are gathered in Table 1.

Table 1

Initial parameters for both studied materials

Parameter	Description	Benchmark	WST-MZ1-S1450G
σ_f [MPa]	Cohesive strength	1.7	3.8
J_c [J/m ²]	Fracture energy	108	286
R	NOD vs. CMOD ratio at ultimate load	2.6	2.6
c	Slope for the post-peak NOD vs. CMOD affine trend	1.54	1.54
BCc	Boundary condition correction	1	1
E [GPa]	Young's modulus	17	65

3. Benchmark case

The present methodology was first applied to one WST in which both NOD and CMOD were measured (Figure 1(a,b)). Moreover, the CZM parameters could be compared with the values from the very same monotonic test reported in Ref. [22], in which the identification was performed using only force data since the simulations were driven by the measured CMOD. Although the geometry for the FE analysis is not entirely on the image frame, a large portion of the specimen that was imaged was available. One important source of independent information to check was displacement fields and gray level residuals as discussed hereafter. The mesh used in Ref. [22] was also considered but CMODs were obtained by extrapolating NOD measurements using Equations (10) and (11) to obtain the boundary conditions to be applied on two nodes (see blue circles in Figure 1(a,b)). However, the parameters for such extrapolations will be considered unknown to simulate one case where the CMOD was not visible (Figure 1(c)). Last, the standard uncertainty $\sigma_F = 5$ N was obtained from the force fluctuations and $\sigma_{\text{NOD}} = 0.5$ centi-px ($\equiv 0.24$ μm) from NOD measurements (via DIC) for images in the pre-loaded step.

Before starting the identification procedure itself, a sensitivity analysis was performed [37]. In the present case, it consisted in analyzing the temporal changes of each column of the sensitivity matrices $[\mathbf{S}_F]$ and $[\mathbf{S}_{\text{NOD}}]$, namely, for each parameter to be calibrated. Further, these sensitivities were first analyzed for the whole set of (360) images and then on a reduced set (one in ten images). Figure 3 shows the temporal changes of all sensitivities for the front face analysis in the converged state. They did not change qualitatively between each iteration and for each specimen side.

The parameter BCc affects more the force at the start of the test, which was expected since it accounts for a correction for the unknown load-free configuration. It is followed by c , R , and E . The cohesive strength σ_f influences the force in the time steps close to the peak load, while J_c is dominant in the post-peak regime.

For the NOD, it is possible to see different trends, complementary to the force sensitivities, although considerably dominated by the parameter c , whose sensitivity increases linearly with the same slope until the end while most of the other parameters exhibit post-peak plateaus. Moreover, after 1.7 mm, a fluctuation of the NOD sensitivities of R and BCc parameter occur. These fluctuations are probably related to numerical issues when very few cohesive elements are still carrying the load. Interestingly, using only one tenth of the available images was sufficient for faithfully describing the sensitivities, and possibly even less images could be used in this first analysis.

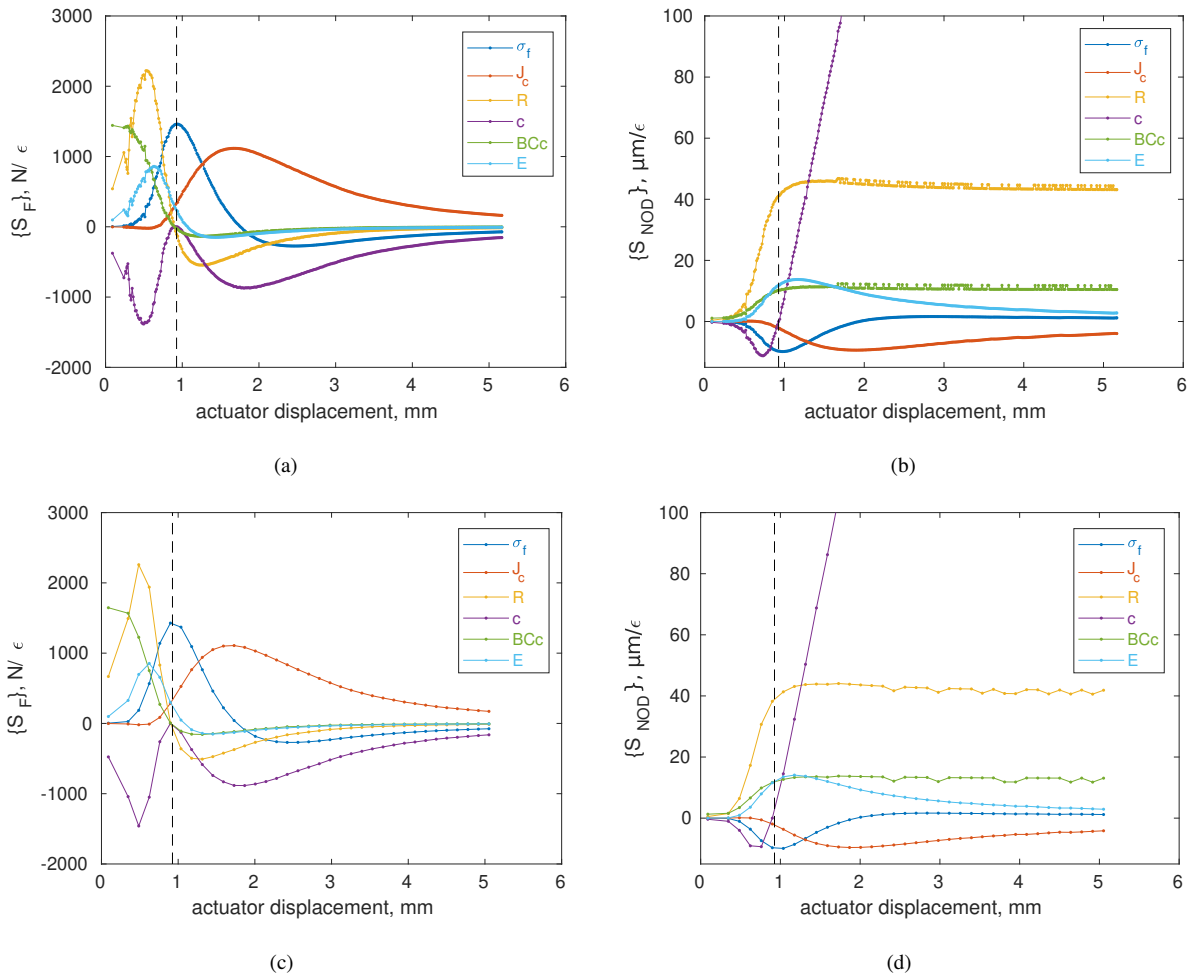


Figure 3: Parameter sensitivities of splitting force $\{S_F\}$ (a,c) and to the NOD $\{S_{NOD}\}$ (b,d) for the front face using the whole image set (a,b) or one tenth of the latter (c,d). The vertical dashed line depicts the ultimate load instant.

Similarly, Figure 4 shows the temporal changes of each column of $[S_F]$ and $[S_{NOD}]$ for the back face in the con-

verged state. They are qualitatively very close to those shown for the front face in Figure 3. The quantitative differences are related to loading imperfections such as wedge misalignment throughout the experiment. The same oscillations are seen for the NOD sensitivities of R and BCc in the post-peak regime, which reinforces the hypothesis that this effect be correlated to the damage state of the cohesive elements.

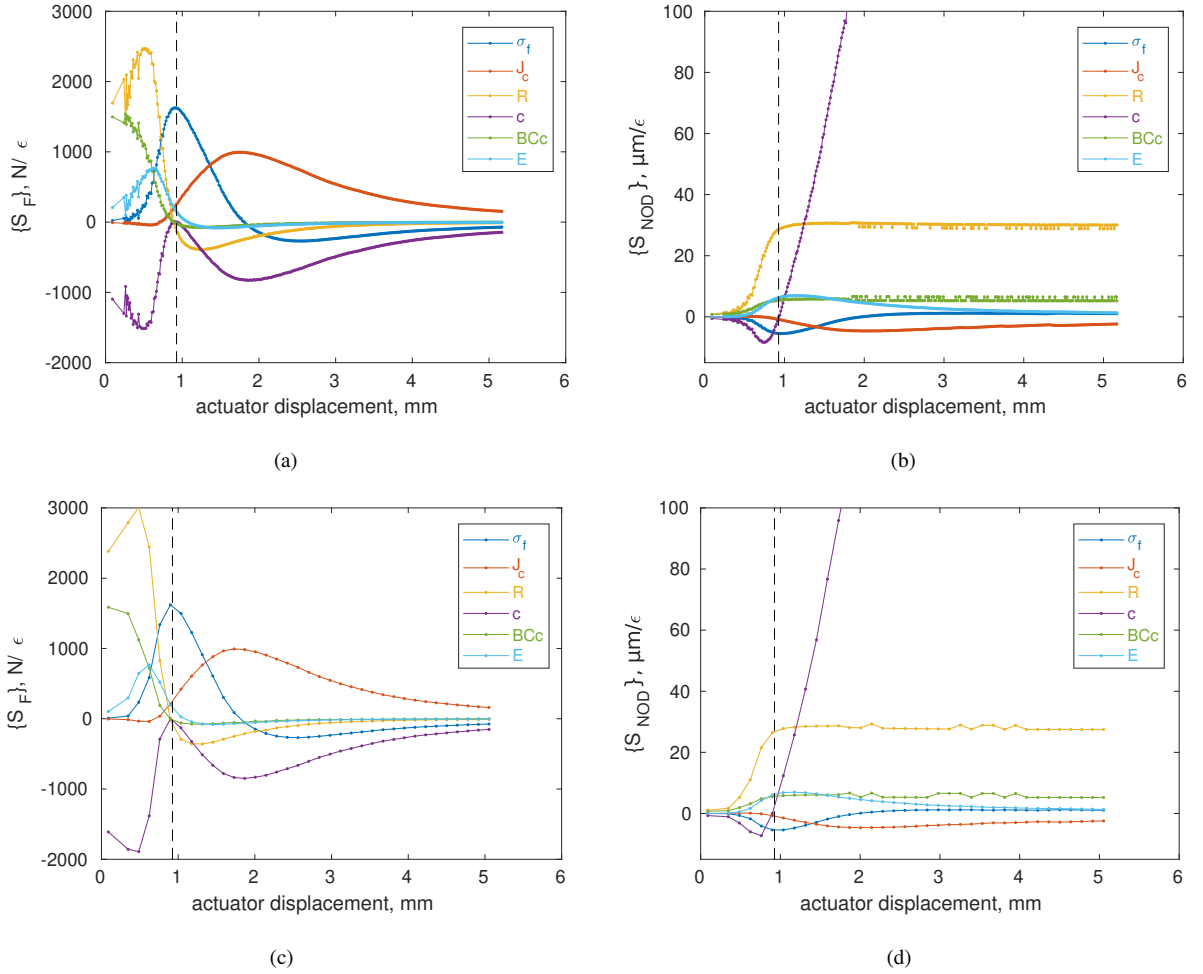


Figure 4: Parameter sensitivities of splitting force $\{S_F\}$ (a,c) and to the NOD $\{S_{NOD}\}$ (b,d) for the back face using the whole image set (a,b) or one tenth of the latter (c,d). The vertical dashed line depicts the ultimate load instant.

The Hessian $[\mathbf{H}]$ and covariance $[\mathbf{C}]$ matrices, as well as the eigen decomposition of $[\mathbf{H}]$ are reported in Figure 5 for the front face. The eigen values reported in Figure 5 span over four orders of magnitude, which shows a reasonable conditioning of the system. If only the four most sensitive eigen parameters were considered, the conditioning becomes even better with only two orders of magnitude. The eigen vectors show small correlations between parameters. The main difference between the matrices calculated using the whole set of images or only few of them is one order of magnitude shift, but they remain qualitatively similar. This factor 10 between both covariance matrices allows us to

anticipate that parameter uncertainties will decrease when using all images. This result may also be used as a way to estimate how many images would be required for a given accuracy, once the test is selected for the material of interest.

From the Hessian matrix $[\mathbf{H}]$ alone, it is possible to infer that the highest sensitivity comes from the parameter c , which is essentially the sixth eigen vector (*i.e.*, related to the highest eigenvalue). The ordering of sensitivities for the other parameters is not straightforward by analyzing $[\mathbf{H}]$. However, it is easily obtained from the eigen vectors, and in decreasing order importance are the following parameters: R , J_c , σ_f , BCc and E . This analysis highlights that using NODs alone, the CMOD may be estimated using the proposed proposed framework, and it is very well conditioned to obtain the needed extrapolation. Moreover, the CZM parameters are also well conditioned, having the highest sensitivities after c and R . The parameter BCc was expected to have a lower sensitivity since it implies a constant displacement, which is more important on the first time steps where displacement is very small and its influence vanishes as the test proceeds. One last point is related to the Young's modulus E , which is the most difficult and uncertain parameter. If the cost function only contained the force measurements, the conditioning would have deteriorated to a point that it became meaningless to calibrate it.

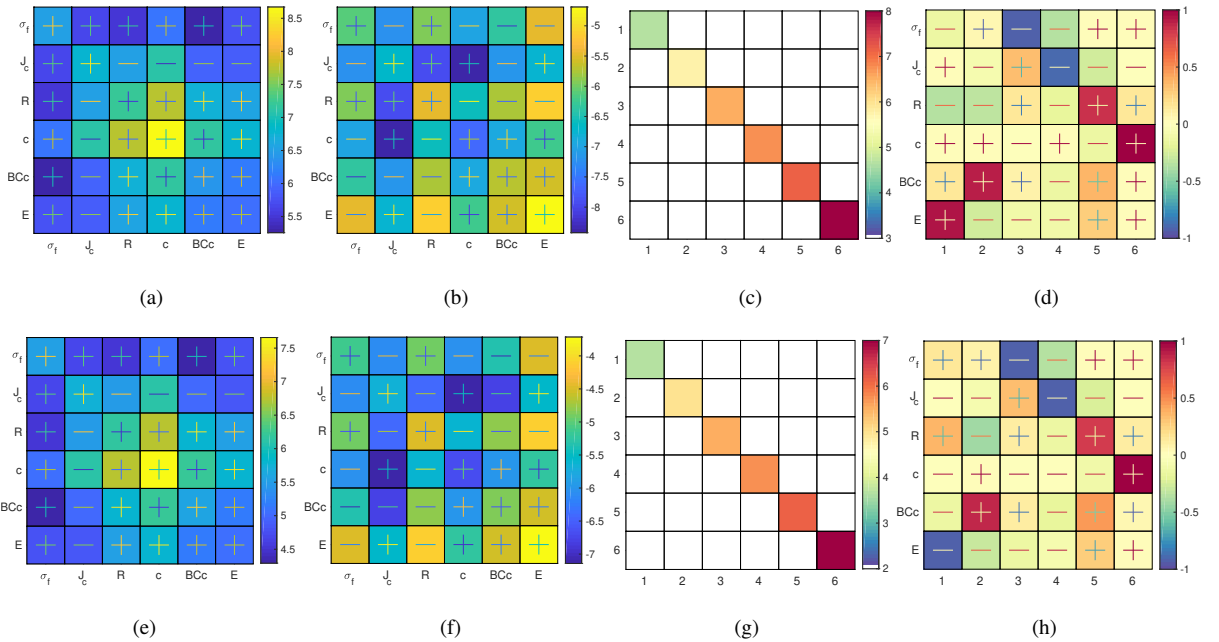


Figure 5: Dimensionless Hessian (a,e) and covariance (b,f) matrices. Diagonal (c,g) and eigen vector (d,f) matrices of the Hessian matrix. The matrices are shown for the whole image set (a-d) and a reduced set (e-h) for the front surface. The first three matrices are shown in decimal logarithms. The components that may have negative values are shown with the signs represented on it.

These same matrices were calculated for the back face and are reported in Figure 6. All the trends are very similar, as expected from the previously reported sensitivity analysis. For the back face however, the eigen decomposition leads

to the third and fourth eigen vectors related to linear combinations of σ_f and J_c , which reinforces that their sensitivity level is close. When using fewer images, there is also a correlation between the parameters BCc and E in the first and second eigenvector, which indicates that using more frames could be helpful to calibrate these lower sensitivity parameters. A similar factor 10 is obtained between both covariance matrices (using all or few images), which will also lead to lower parameter uncertainties.

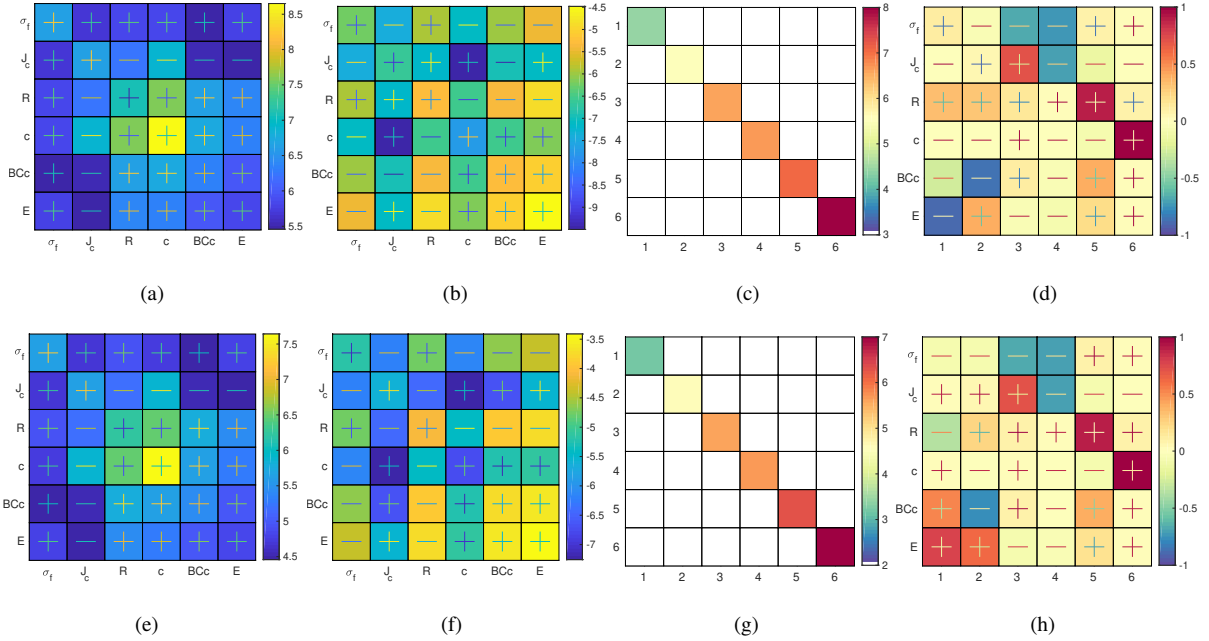


Figure 6: Dimensionless Hessian (a,e) and covariance (b,f) matrices. Diagonal (c,g) and eigen vector (d,f) matrices of the Hessian matrix. The matrices are shown for the whole image set (a-d) and a reduced set (e-h) for the back surface. The first three matrices are shown in decimal logarithms. The components that may have negative values are shown with the signs represented on it.

Experimental and simulated force and NOD curves are displayed for the front face analyzes in Figure 7. A very good agreement is observed (*i.e.*, ≈ 40 N) with errors only about eight times the force uncertainty (also accounting for servohydraulic fluctuations), and six times the uncertainty related to NOD measurements (*i.e.*, ≈ 1.5 μm). It is worth noting that $\chi_F = 2.9$ was reported in Ref. [22], but with a higher level for σ_F (*i.e.*, based on 0.1% of the load cell capacity, or 29 N). After adding the NOD data in the identification procedure, it achieved an even better description of the horizontal force (*i.e.*, it would have been equal to 16 with the present load uncertainty). The latter was very well captured for the pre-peak regime, apart from the very beginning where the noise to signal ratio was very high. In the post-peak regime, the simulation follows the trend of the experimental curve, although slightly underestimating it overall, and overestimating it only between 1.5 and 2.2 mm of actuator displacement. It is worth noting that the shape of the cohesive law was kept constant. Although out of the scope of the present work, further investigation on that

parameter (for the same PPR cohesive law) may help to achieve even better agreement with experimental results. For the NOD, some very small differences are seen at the beginning of the affine trend but the overall trend is very well captured by the simulations. Moreover, the coarser temporal discretization using few images led to really close results, which also emphasizes how using only a fraction of the total data could be sufficient to achieve good results in the present case.

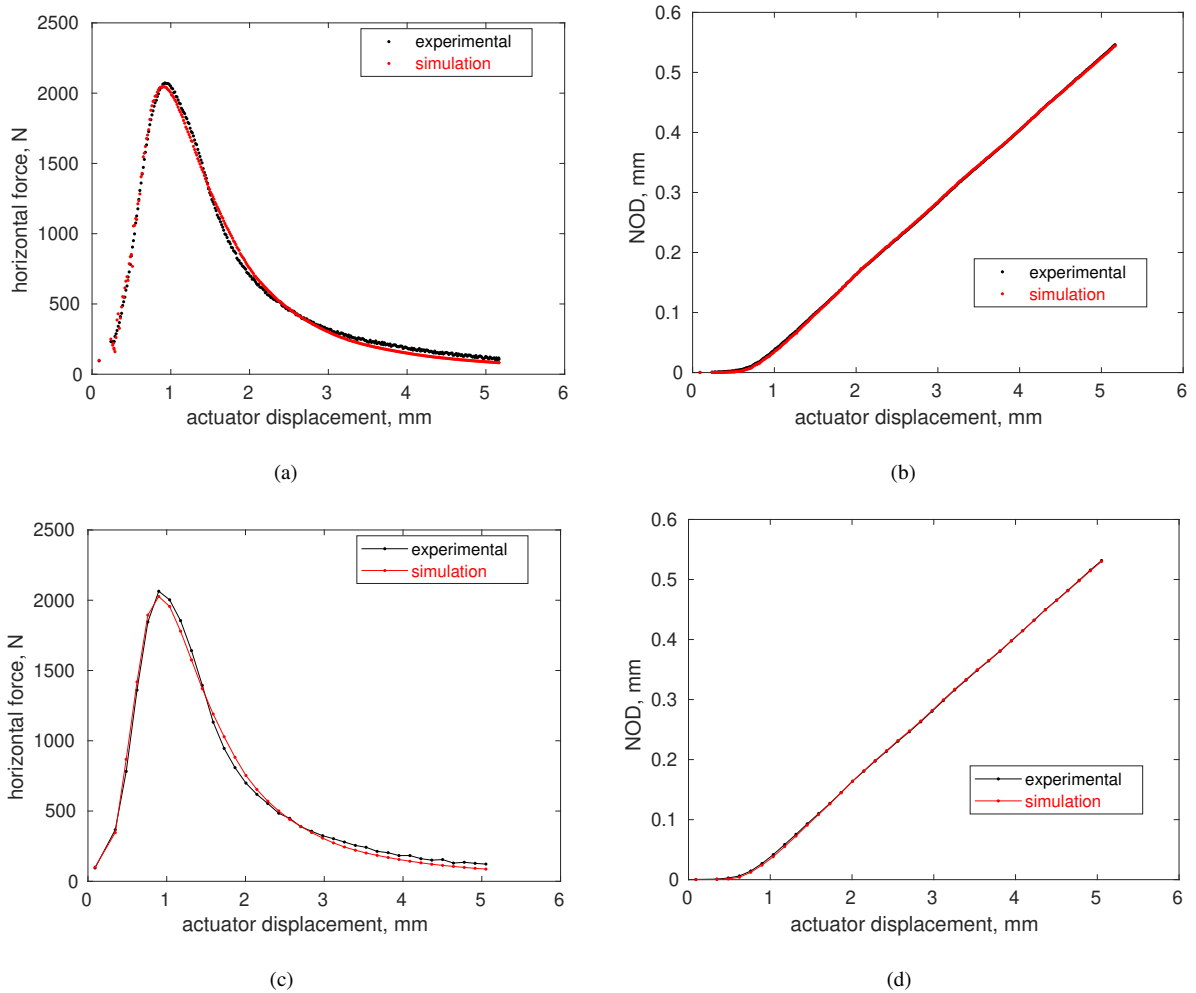


Figure 7: Experimental and simulated force (a,c) and NOD (b,d), using the full image set (a,b) or only a few images (c,d) for the front face.

Similar experimental and simulated forces, as well as NODs analyzed for the back face are shown in Figure 8. A slightly higher χ_F is observed especially for the case using all images (*i.e.*, $\chi_F = 9.7$), which is related to the higher oscillations at the beginning of the test. Imperfections of the sample geometry and wedge misalignment may cause one side to experience more load at the very beginning of the experiment before crack propagation. This effect induces a decrease of χ_F when fewer images are considered (*i.e.*, only one image of the very beginning of the test was used).

For the NODs, χ_{NOD} is even smaller for the back face ($\chi_{NOD} = 3.2$ in both cases) and no specific difference between both curves is observed.

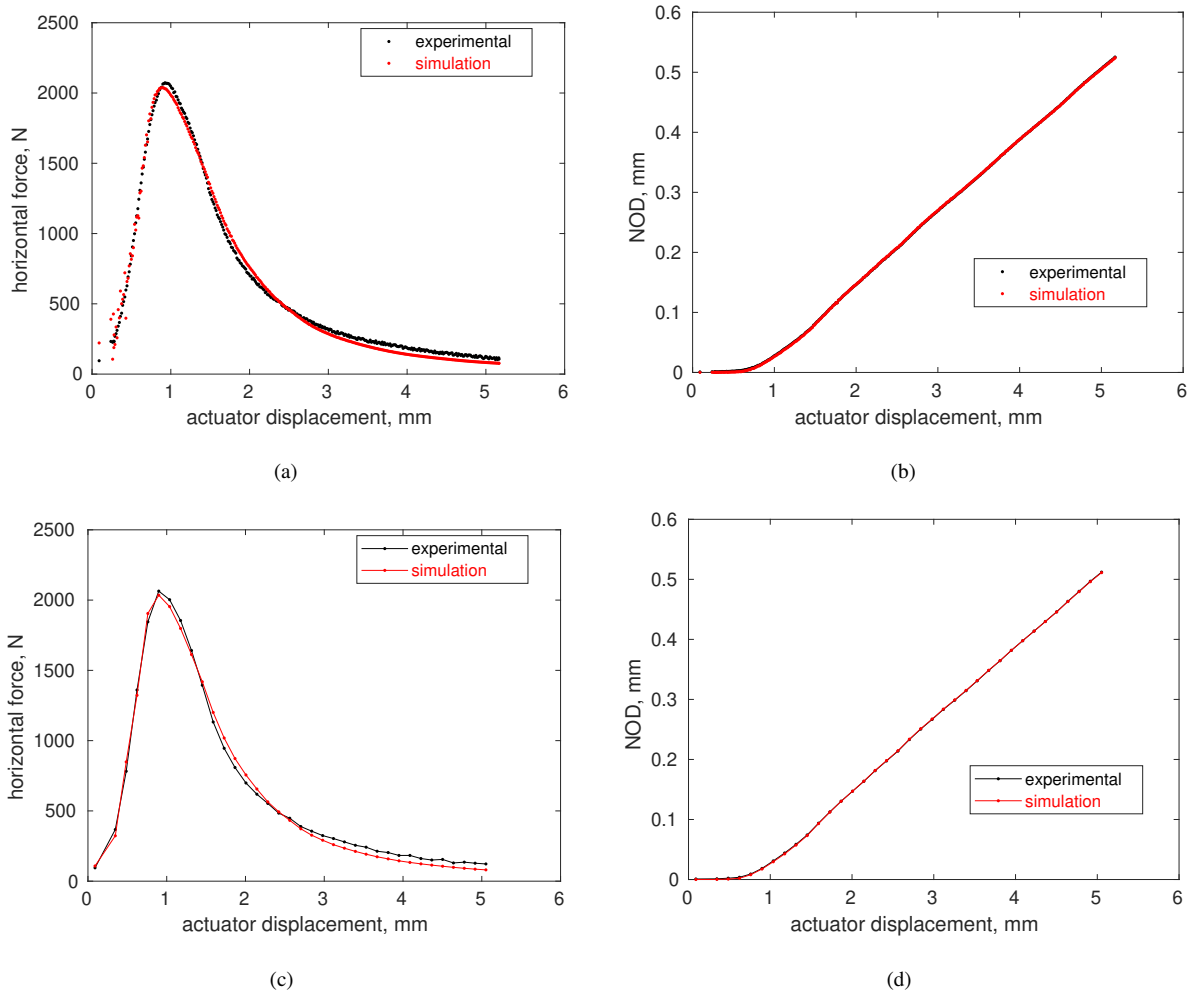


Figure 8: Experimental and simulated force (a,c) and NOD (b,d), using the full image set (a,b) or only a few images (c,d) for the back face.

The parameters calibrated when analyzing the front and back faces are reported in Table 2. The set of reference parameters is also given from the identification performed with CMOD data utilized as boundary conditions, and for the experimental relationship between NOD and CMOD [22]. For the front face, the parameters obtained using few images are very close to those obtained when using all images. However, their standard uncertainties are about three times higher. This trend was expected from the covariance matrices shown in Figure 5(b,f). The difference in the R parameter may be related to the low number of points in the first steps when few images are used. Comparing the cases where CMOD or NOD were used for driving boundary conditions, σ_f remains virtually the same while J_c increased about 10% for the NOD case. This increase may also be related to different Young's moduli E , which was not calibrated

in the case using CMOD data. The parameters R and c , similar to σ_f , remain very close in both identifications with differences of the order of 1% to 3%. Although a BCc value of 0.82 was necessary in the CMOD-driven case, when NOD data were used it remained closer to unity (*i.e.*, a smaller correction was needed).

Table 2

Converged parameters for both identification with 36 and 360 images for the front and back faces. Standard uncertainties (\pm) are also reported. Reference parameters after Ref. [22].

Parameter	Front face			Back face		
	Ref.	36 images	360 images	Ref.	36 images	360 images
σ_f [MPa]	1.76	1.78 ± 0.005	1.794 ± 0.002	1.67	1.609 ± 0.004	1.610 ± 0.001
J_c [J/m ²]	117	132.0 ± 0.2	132.3 ± 0.06	112	118.7 ± 0.2	118.9 ± 0.06
R	2.31	2.36 ± 0.01	2.272 ± 0.004	2.37	2.31 ± 0.02	2.160 ± 0.005
c	1.54	1.503 ± 0.0007	1.503 ± 0.0002	1.57	1.516 ± 0.0007	1.516 ± 0.0002
BCc	0.82	0.970 ± 0.004	0.975 ± 0.001	0.73	0.73 ± 0.01	0.825 ± 0.002
E [GPa]	–	20.5 ± 0.3	21.2 ± 0.1	–	43.7 ± 0.9	44.0 ± 0.3
χ_F	–	8.3	8.1	–	8.7	9.7
χ_{NOD}	–	6.2	6.1	–	3.2	3.2

The overall observations for the back face are similar, with σ_f now being slightly smaller, and J_c closer to the reference level. Care should be taken to compare J_c since the Young's Modulus is about twice the level reported for the front face. The Young's modulus was expected to be the least sensitive parameter (Figures 5 and 6). Such difference between both faces highlights this point. Higher resolutions or more images in time steps where E is most sensitive could improve this results. Moreover, 3D simulations using information from both opposite sides is another perspective to improve the identification of elastic parameters [38]. The BCc parameter is closer to the CMOD case as well, which is interesting since the higher the needed correction, the more CMOD and NOD are affected instead of only the CMOD, as observed for the front face.

Given the fact that only NOD data were used in addition to load recordings, it was possible to further probe the calibrated CZM with kinematic measurements. Standard T3-DIC was run over the cyan ROIs shown in Figure 1(a,b). From these measurements instantaneous RMS displacement differences normalized by the corresponding measurement uncertainties (*i.e.*, $\chi_u(t)$) are displayed in Figure 9(a,b). There is a gradual increase of both residuals with time, which is due to the assumption of a straight crack path in a sample with no lateral grooves to guide crack propagation. Although out of the scope of the present work, this shortcoming could be improved by using the gray level residuals to position cohesive elements along the actual crack path [39]. Even with such hypothesis, the RMS difference is on average 25

times the displacement uncertainty (*i.e.*, $\approx 24 \mu\text{m}$), which is deemed small given the present conditions.

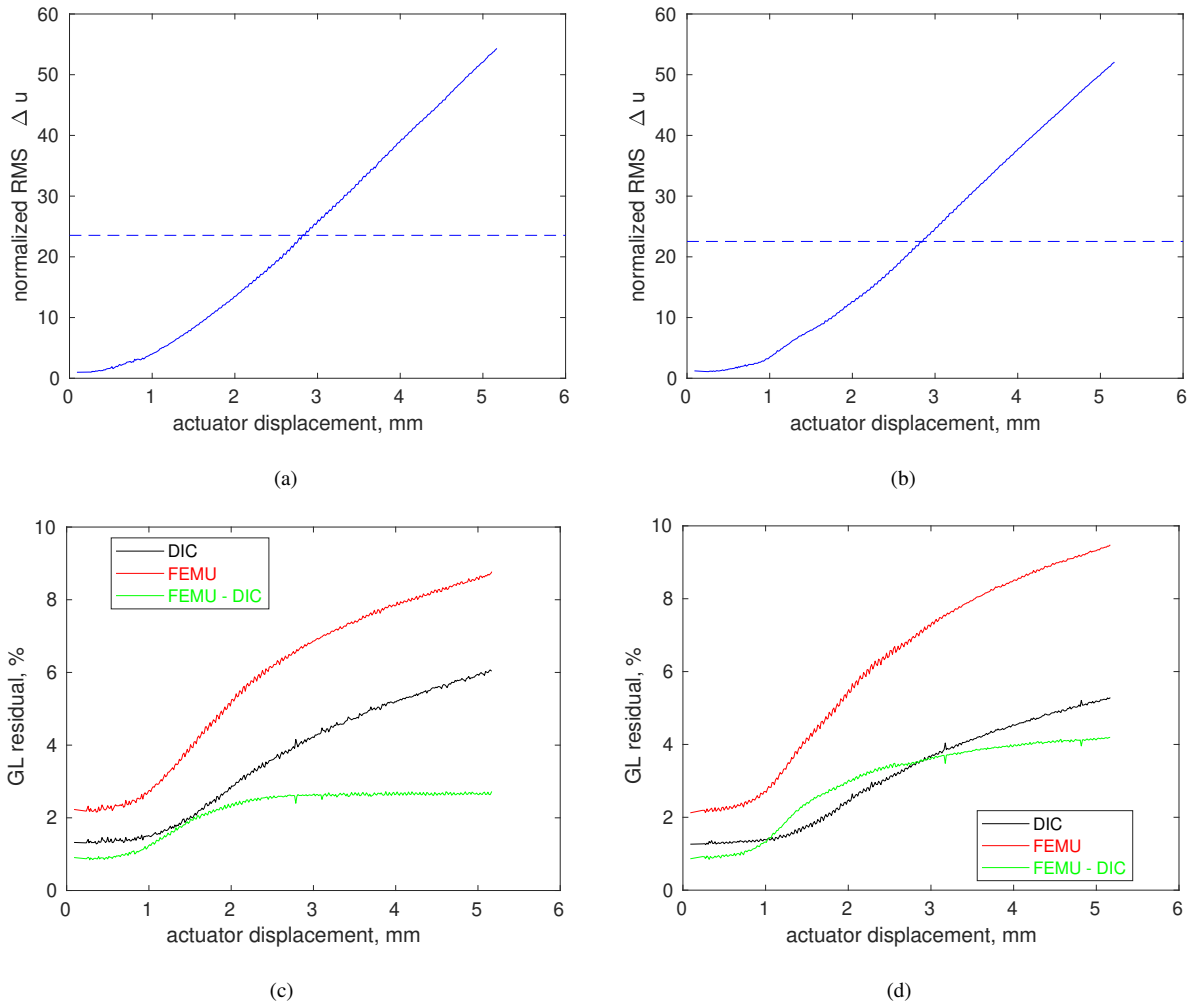


Figure 9: (a,b) Instantaneous RMS residuals between FEMU and DIC displacement fields. (c,d) Corresponding gray level residuals. The results are reported for the front (a,c) and back (b,d) faces.

Figure 9(c,d) shows the change of gray level residuals normalized by the dynamic range of the reference image for the previous DIC analyses. There is a gradual increase that is related to the crack propagating through the sample. These residuals are compared to a new DIC analysis using the displacement fields corresponding to the calibrated parameters augmented by unknown rigid body motions that were then determined in an integrated framework. The new residuals are rather close to the DIC analyses that did not account any mechanical model. Consequently, the kinematic predictions of the calibrated CZM are therefore in rather good agreement with experimental observations.

This benchmark case provided insight into the consistency of NOD usage to guide FE simulations in order to calibrate CZM parameters. Very similar parameters were obtained in comparison to results using only CMOD as boundary conditions. Good conditioning was achieved by coupling force and NOD data in the FEMU cost function.

The proposed simulations capture very well the splitting force and NOD histories, with rather consistent kinematics confirmed by the displacement fields and gray level residual maps. Moreover, not only could the cohesive parameters be calibrated, but also the coefficients for extrapolating NOD data to CMODs, the Young's modulus, and a correction factor for boundary conditions as well. The presented analyses fully validate the procedure that is now applied to a case where the CMOD data were not accessible.

4. WST-MZ1-S1450G experiment

A WST in which the CMOD was not measurable (see Figure 1(c)) is now analyzed. It was a preliminary test at room temperature that was performed before higher temperature experiments [26]. Therefore, the sample was put inside the (turned off) furnace and there was only one quartz window between the camera and the sample. This sample had lateral grooves to guide the crack, meaning that a straight crack path is a good assumption for the present case. The load uncertainty σ_F was equal to 10 N and that of NODs $\sigma_{\text{NOD}} = 1.5$ centi-px (or $\equiv 0.3 \mu\text{m}$). For this test, there were 584 images available during loading (apart from the reference). In order to obtain a first order estimate of the sought parameters, only one in ten images were used (*i.e.*, a total of 59 equally spaced time steps). The identification procedure took about 15 minutes for each iteration and converged in seven iterations. Then, when all images are used with the improved initialization, each iteration lasted two hours and converged in three iterations. Last, a final analysis was run with even less images (*i.e.*, one in 50 images), namely only keeping 12 in the identification framework. Each iteration took five minutes and converged in five iterations, when initialized with the same starting parameters as the case with 59 images (see Table 1).

The results for the sensitivity analyses for the converged state are presented in Figure 10. The overall trends are qualitatively identical to the benchmark case. This consistency is believed to be mostly related to the WST setup, since the materials were very different. Moreover, the benchmark case had no lateral grooves, contrary to WST-MZ1-S1450G, which further proves the robustness of the qualitative sensitivities. To exemplify the benefits of coupling force and NOD data in the cost function, it is worth noting that the fracture energy J_c and c slope show similar post-peak force sensitivities with an opposite trend. When their (very dissimilar) NOD sensitivities are also accounted for, they become decoupled and the conditioning is improved. The case using only 12 images shows that such a coarse discretization can already qualitatively capture all sensitivity features.

On the Calibration of Cohesive Parameters from NODs in WSTs

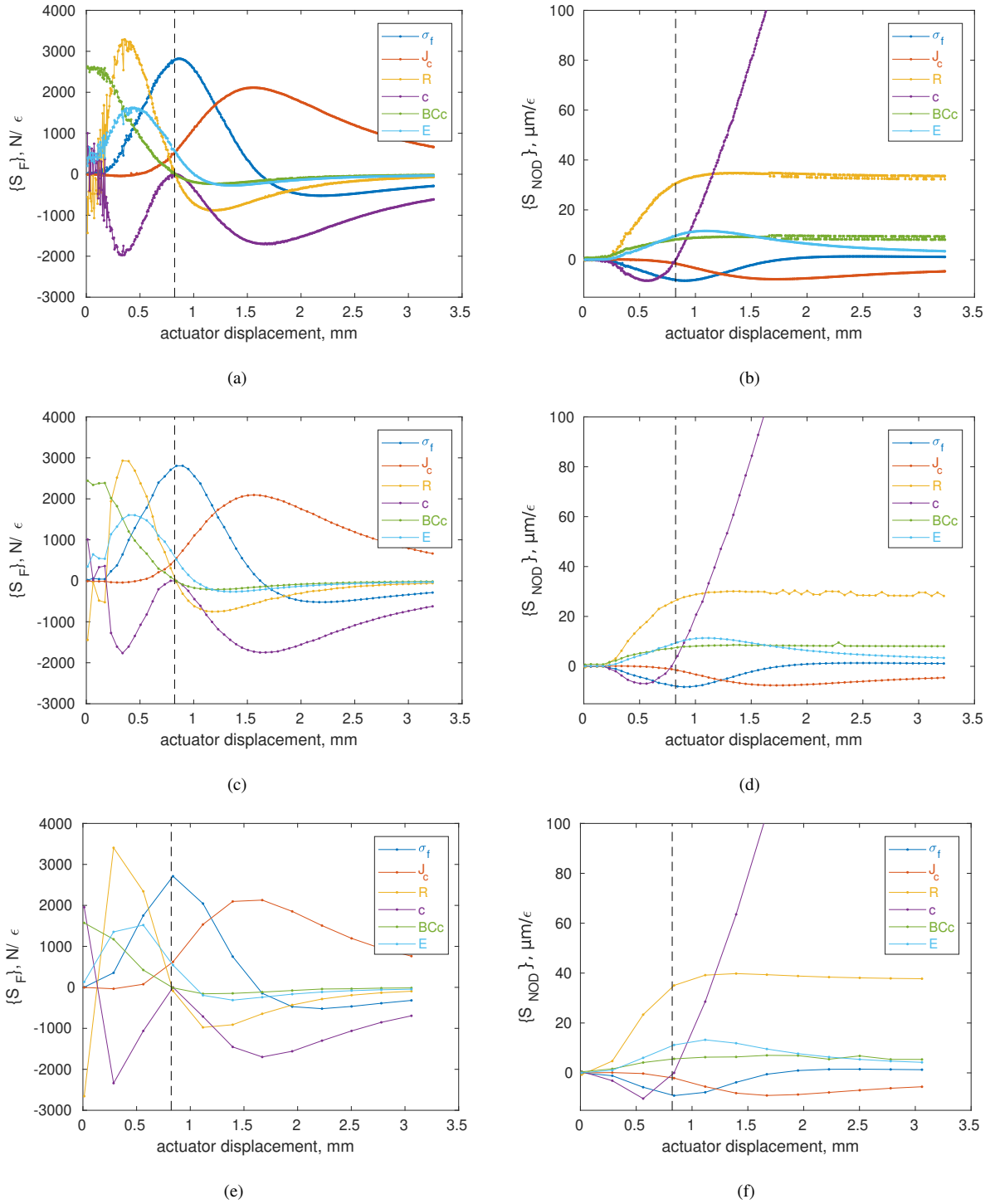


Figure 10: Parameter sensitivities of splitting force $\{S_F\}$ (a,c,e) and NOD $\{S_{NOD}\}$ (b,d,f) using the whole (584) image set (a,b), 59 (c,d) or 12 (e,f) images from the full set of WST-MZ1-S1450G. The vertical dashed line depicts the ultimate load instant.

The Hessian matrix $[H]$ and its diagonalization are reported in Figure 11 along with the covariance matrix $[C]$. The conditioning for WST-MZ1-S1450G is better than the benchmark cases, given the fact that the eigen values span over three orders of magnitude. The covariance magnitude also changes by a factor 10 when 59 images are used instead of the whole set, and then fivefold when only 12 images. The same ordering of parameter importance is observed as in the benchmark case, with the c and R parameters coming first, followed by the CZM ones, BCc and then the Young's modulus E . Interestingly, when using only 12 images, the eigenvectors show smaller correlations between parameters (e.g., second and fifth eigen vectors).

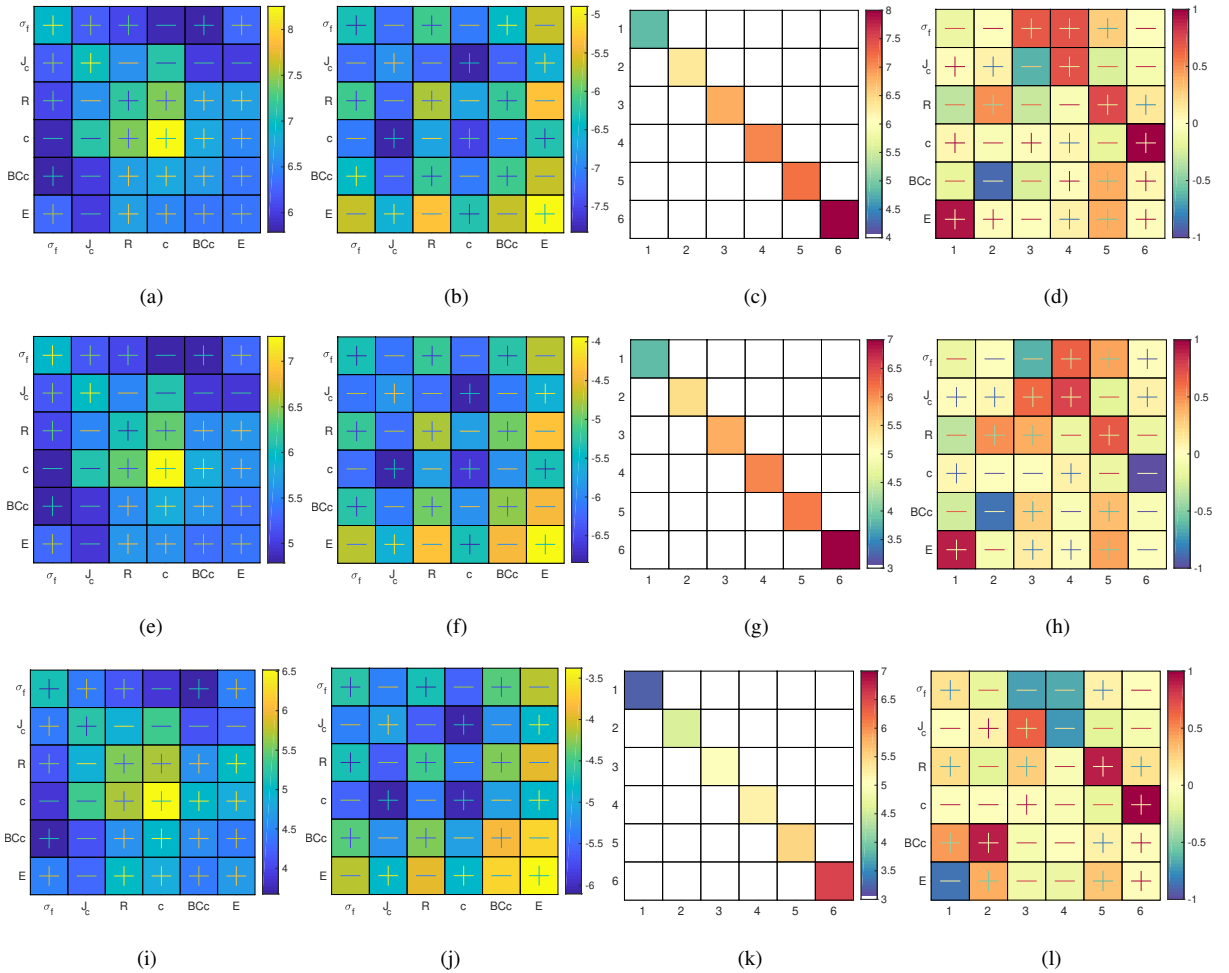
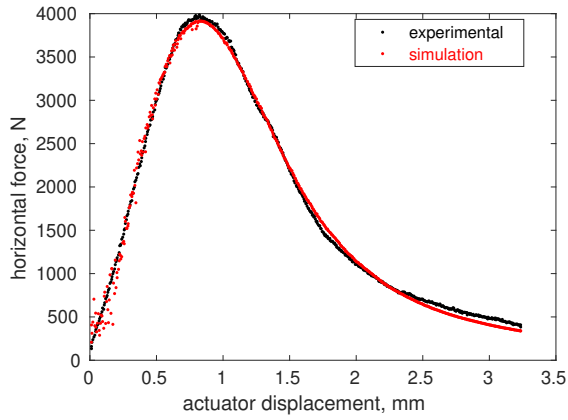


Figure 11: Dimensionless Hessian (a,e,i) and covariance (b,f,j) matrices of WST-MZ1-S1450G. Diagonal (c,g,k) and eigen vector (d,f,l) matrices of the Hessian matrix. The matrices are shown for the analysis using 584 (a-d), 59 (e-h), and 12 (i-l) images. The first three matrices are shown in decimal logarithms. The components that may have negative values are shown with the signs represented on it.

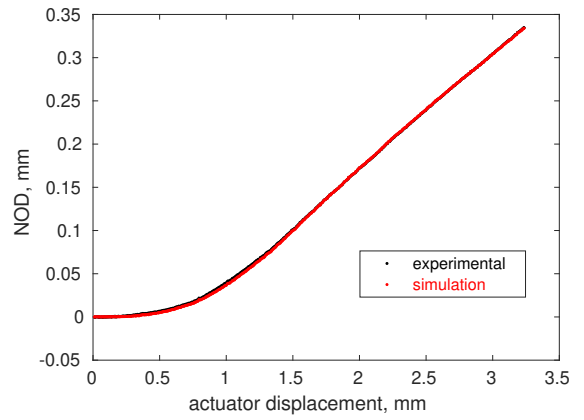
Both experimental and simulated splitting forces as well as NODs are shown in Figure 12 for the three identi-

fications. Their goodness of fit measured by χ_F and χ_{NOD} ranges between 2.5 and 10, being better when only 12 images were used, deteriorating a bit using 59 images but being further improved when all the images were considered (Table 3). Apart from oscillations at the beginning of the test, the loading curve mainly shows small deviations below 50% of the ultimate load in the post-peak regime. Therefore, most of the crack initiation and propagation process is well captured with the selected CZM. Small deviations in the post-peak regime are observed, similar to the benchmark case. Although out of the scope of the present work, cohesive laws of slightly different shapes may be able to further improve such fit. For the NOD data, the agreement of the curves is excellent, with some very small deviations around 1 mm of actuator displacement (Figure 12(d)). The difference between experimental and simulated peak loads is less than 2% in all three cases, which shows that initiation is also consistently described.

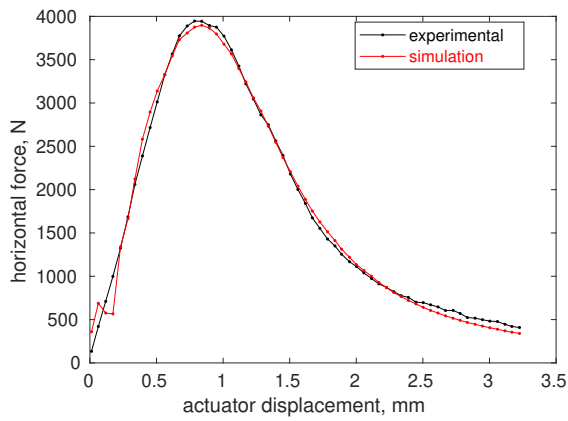
On the Calibration of Cohesive Parameters from NODs in WSTs



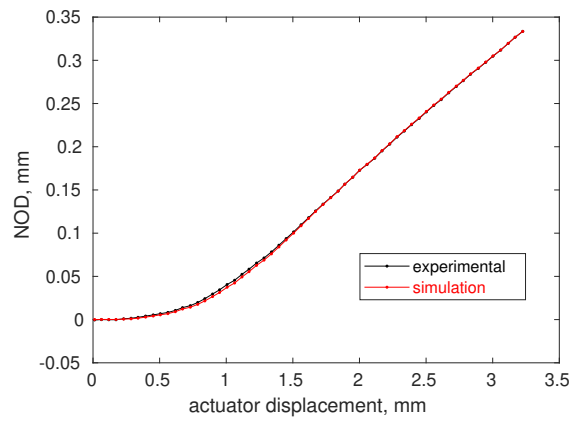
(a)



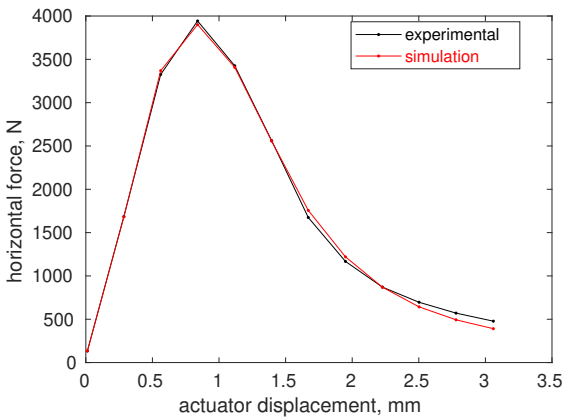
(b)



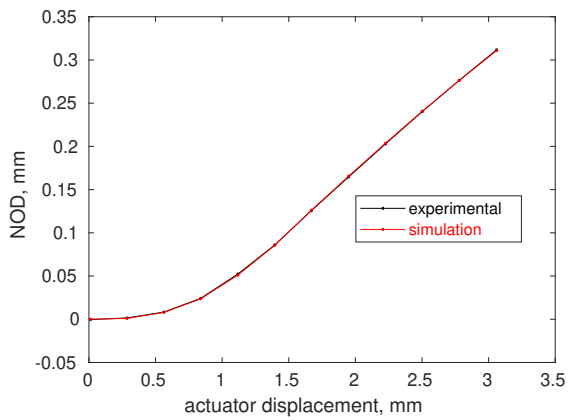
(c)



(d)



(e)



(f)

Figure 12: Experimental and simulated force (a,c,e) and NOD (b,d,f) histories using the full (584) image set (a,b), 59 (c,d), or 12 images (e,f) of WST-MZ1-S1450G.

The calibrated parameters for the three identifications are shown in Table 3. These results show how robust the

identification procedure was since all the parameters were very close even using very few images. This result is due to the good conditioning of the Hessian (Figure 11(c,g,k)). When 12 images were used, among all parameters the Young's modulus E is the farther to that obtained with the full image set (with a 15% difference), followed by σ_f and J_c with differences of 3% and less than 1%, respectively. When 59 images were selected, these differences were reduced to an order of 1% or below. These results can be used as guidelines for data acquisition during similar experiments and optimizing identification procedures, depending on the sought parameters, which was not straightforward before the present sensitivity analyses. The value $BCc > 1$ means that a tensile correction was needed, which indicates that some compressive state was present in the reference image that is believed to be related to wedge misalignment, especially considering the setup inside the furnace [26].

Table 3

Converged parameter sets for identifications using 12, 59 and 584 images with respective standard uncertainties (\pm).

Parameter	12 images	59 images	584 images
σ_f [MPa]	4.40 ± 0.02	4.25 ± 0.009	4.288 ± 0.003
J_c [J/m ²]	284 ± 0.8	281.6 ± 0.3	282.6 ± 0.1
R	2.31 ± 0.01	2.16 ± 0.009	2.156 ± 0.003
c	1.448 ± 0.001	1.474 ± 0.0007	1.4668 ± 0.0002
BCc	1.57 ± 0.02	1.340 ± 0.005	1.263 ± 0.001
E [GPa]	40 ± 0.8	47.0 ± 0.5	46.4 ± 0.2
χ_F	4.4	9.8	8.2
χ_{NOD}	2.5	5.0	4.2

The standard uncertainties are also reported in Table 3. As expected, as more images are considered in the identification procedure, the uncertainties are lowered. Using only 12 images yields uncertainties one order of magnitude (*i.e.*, $\approx \sqrt{50}$) higher than the case using the full data set. The case using 59 images had standard uncertainties about three times (*i.e.*, $\approx \sqrt{10}$) higher than that with 584 images, thereby corroborating what was observed in the benchmark case. It is also worth noting that the R parameter changed considerably when only 12 images were used. As seen in Figure 7(d,h,l), the influence of the R parameter is the highest in for fifth eigen vector. The third row of the eigen vector matrices correspond to the influence of the R parameter on each eigen vector. For the case with 59 and 584 images, its influence in the other eigen vectors is not negligible (*e.g.*, in the second eigen vector coupled to BCc). When more images are added, the finer temporal sampling brings more uncorrelated information, which was not captured with 12 images. To exemplify this point, one may check the force sensitivity of R and BCc parameters in Figure 10. When using 59 or 584 images (*i.e.*, Figures 10(a,c)), the BCc sensitivity goes downward from the start, while R in-

creases until $t \approx 500$ s. If this tendency is compared to the case with 12 images (Figure 10(e)), apart from the first image, both curves show very similar trends apart from one multiplicative factor between them (*i.e.*, are essentially anti-correlated). Therefore, using more images led to more trustworthy parameters, since their full and detailed effects were better captured.

As for the benchmark case, the predictive quality of the model was further probed with additional DIC analyses. Figure 13(a) shows the displacement residual between DIC and FEMU kinematics, normalized by the displacement uncertainty when compared in the cyan region of Figure 1. The grooved region (Figure 1(c)) was not accounted for in these calculations since the darker regions had very low contrast and the corresponding results would not be trustworthy. On average, the RMS displacement difference ($6 \mu\text{m}$ or 0.32 px) is 16 times the uncertainty level (0.02 px). The two displacement fields are probed independently thanks to the gray level residuals (Figure 13(b)). The difference between both gray level residuals is on average less than 1% of the dynamic range, which is even lower than what was observed in the benchmark case (Figure 9). As the crack was guided by the lateral grooves in WST-MZ1-S1450G, the crack path was better described by the assumption of a straight propagation, which explains the smaller residual levels and differences in the present case.

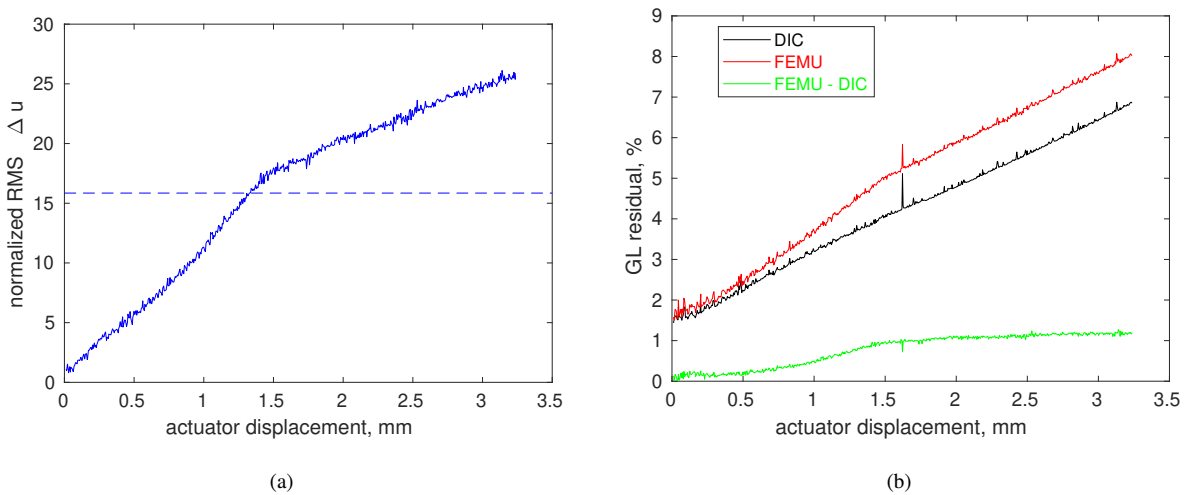


Figure 13: (a) Instantaneous RMS residual between FEMU and DIC displacement fields. (b) Corresponding gray level residuals.

5. Conclusion

Cohesive zone model (CZM) parameters were calibrated using notch opening displacements (NODs) and force data from wedge splitting tests (WSTs). One benchmark case was first evaluated to validate the methodology, since the crack mouth opening displacements (CMODs) and images of both opposite faces were available. Then, a WST that had only the NOD visible (and only for one side) was analyzed. The proposed framework was especially interesting

when imaging the crack propagation path (to have better access to data related to the fracture process zone) without losing information about the loading conditions for driving numerical simulations. Not only were CZM parameters calibrated, but also three parameters related to the boundary conditions together with the Young's modulus. Overall, the numerical results showed a good agreement with experimental data in terms of force, NODs, displacements fields, and gray level residuals. They showed that the selected CZM [31] was able to capture the main features of crack initiation and propagation in the two refractories studied herein.

The sensitivity analyses showed how each parameter influenced the splitting force and NODs, which were coupled in the cost function for identification purposes. By analyzing the Hessians and their diagonalized counterparts, the conditioning of the present framework could be assessed, as well as the correlation between parameters and also their influence. The diagonal of the covariance matrix also gave access to the uncertainties for the calibrated parameters. The parameters in decreasing order of importance, for each analyzed case, were c and R (related to extrapolating NOD to CMOD), followed by σ_f and J_c (CZM parameters), then BCc (a correction for the boundary condition) and E (Young's modulus). If force or NOD alone had been used in the cost function, the conditioning would have deteriorated to a point that the calibration of some (if not all) the chosen parameters would not be trustworthy. Further, the effect on the calibration results of using only few images of the whole set was also investigated. Although very few images (down to 12) could be used (in particular to get initial estimates), the more time steps were used the more trustworthy the results and the higher the influence of each parameter.

On the benchmark case, it was shown that very similar results were obtained if NODs were used instead of CMODs to drive the boundary conditions in the simulation, thereby validating the proposed methodology. Analyzing both faces gave insight into the variability of calibrated parameters. Although the cohesive strength and the fracture energy were very similar, the Young's modulus had larger deviations, which are presumably related to 3D effects during loading and crack propagation [38]. Consequently, it is advised to analyze both sides whenever possible, especially if the elastic parameters are sought. For the other WST, first estimates for the CZM parameters were obtained by simulating the full sample even if only part of it was imaged. In that case, there were lateral grooves guiding the crack, which further improved the kinematic residuals (*i.e.*, in displacement and gray level) under the hypothesis of straight propagation.

Last, the absence of CMOD data in the last WST-MZ1-S1450G was due to the sample being inside a turned off furnace with limited size window. It was a preliminary test before higher temperature tests were performed [26]. Therefore, using the same framework for these experiments would be a direct continuation of the present work to compare the parameters for the same material but at 600°C. 3D analyzes to better understand crack propagation and especially the influence on elastic parameters is another perspective, although information from both opposite faces would be needed.

Acknowledgments

This study was financed in part by the Coordenação de Aperfeiçoamento de Pessoal de Nível Superior - Brasil (CAPES) - Finance Code 001 CAPES (Brazil) and #2018/15266-0, #2018/23081-0, and #2010/20920-9, São Paulo Research Foundation (FAPESP). The authors would like to thank Prof. J.A. Rodrigues for stimulating discussions about various aspects of WSTs and IBAR (Indústrias Brasileiras de Artigos Refratários, Poá, Brazil) for kindly providing the materials.

Credit authorship statement

R. Vargas: Conceptualization, Methodology, Investigation, Software, Original draft preparation, Writing - Review & Editing

R.B. Canto: Supervision, Conceptualization, Writing - Review & Editing, Resources, Funding acquisition, Project administration

F. Hild: Supervision, Conceptualization, Methodology, Software, Formal analysis, Writing - Review & Editing, Resources, Funding acquisition, Project administration

Declaration of Competing Interest

The authors declare that they have no known competing financial interests or personal relationships that could have appeared to influence the work reported in this paper.

References

- [1] W. E. Lee, W. Vieira, S. Zhang, K. Ghanbari Ahari, H. Sarpoolaky, C. Parr, Castable refractory concretes, *International Materials Reviews* 46 (3) (2001) 145–167.
- [2] P. Luz, A., A. L. Braulio, M., C. Pandolfelli, V., *Refractory Castable Engineering*, 1st Edition, Vol. 1, Göller Verlag, São Carlos, SP, 2015.
- [3] J. Wachtman, *Materials and Equipment - Whitewares - Refractory Ceramics - Basic Science: Ceramic Engineering and Science Proceedings*, Volume 16, no. 1 in *Ceramic Engineering and Science Proceedings*, Wiley, 2009.
- [4] W. E. Lee, R. E. Moore, Evolution of in situ refractories in the 20th century, *Journal of the American Ceramic Society* 81 (6) (1998) 1385–1410.
- [5] R. W. Steinbrech, Toughening mechanisms for ceramic materials, *Journal of the European Ceramic Society* 10 (3) (1992) 131–142.
- [6] R. O. Ritchie, The conflicts between strength and toughness, *Nature materials* 10 (11) (2011) 817.
- [7] M. A. J. Van Gils, L. J. M. G. Dortmans, G. De With, W. A. M. Brekelmans, J. H. P. De Vree, Size effect predictions by fracture models for a refractory ceramic, *International journal of fracture* 75 (3) (1996) 273–283.
- [8] D. Dugdale, Yielding of steel sheets containing slits, *J. Mech. Phys. Solids* 8 (1960) 100–104.
- [9] G. Barenblatt, The mathematical theory of equilibrium of crack in brittle fracture, *Adv. Appl. Mech.* 7 (1962) 55–129.
- [10] A. Hillerborg, M. Modéer, P. E. Petersson, Analysis of crack formation and crack growth in concrete by means of fracture mechanics and finite elements, *Cement and Concrete Research* 6 (6) (1976) 773–782.

- [11] B. Cotterell, S. W. Ong, C. Qin, Thermal shock and size effects in castable refractories, *Journal of the American Ceramic Society* 78 (8) (1995) 2056–2064.
- [12] K. Andreev, H. Harmuth, FEM simulation of the thermo-mechanical behaviour and failure of refractories—a case study, *Journal of Materials Processing Technology* 143 (2003) 72–77.
- [13] E. Jiménez-Piqué, A. Dortmans, G. de With, Fictitious crack modeling of the fracture of a refractory ceramic: fitting through experimental measurements of the displacement field around the fracture process zone, in: *Key Engineering Materials*, Vol. 264, Trans Tech Publ, 2004, pp. 1759–1762.
- [14] J.-D. Mathias, N. Tessier-Doyen, Homogenization of glass/alumina two-phase materials using a cohesive zone model, *Computational materials science* 43 (4) (2008) 1081–1085.
- [15] I. Özdemir, W. A. M. Brekelmans, M. G. D. Geers, Modeling thermal shock damage in refractory materials via direct numerical simulation (DNS), *Journal of the European Ceramic Society* 30 (7) (2010) 1585–1597.
- [16] J. Hein, O. El Khatib, M. Kuna, Influence of interfaces on crack propagation through a layered refractory loaded by thermal shock, *JOURNAL OF CERAMIC SCIENCE AND TECHNOLOGY* 7 (2) (2016) 203–208.
- [17] D. Gruber, H. Harmuth, A laser irradiation disc test for fracture testing of refractory fine ceramics, *Journal of the European Ceramic Society* 34 (15) (2014) 4021–4029.
- [18] S. Jin, D. Gruber, H. Harmuth, R. Rössler, Thermomechanical failure modeling and investigation into lining optimization for a Ruhrstahl Heraeus snorkel, *Engineering Failure Analysis* 62 (2016) 254–262.
- [19] L. Pan, Z. He, Y. Li, B. Li, S. Jin, Inverse simulation of fracture parameters for cement-bonded corundum refractories, *JOM* 71 (11) (2019) 3996–4004.
- [20] R. Vargas, J. Neggers, R. B. Canto, J. A. Rodrigues, F. Hild, Analysis of a castable refractory using the wedge splitting test and cohesive zone model, *Journal of the European Ceramic Society* 39 (13) (2019) 3903–3914.
- [21] A. Doitrand, R. Estevez, M. Thibault, P. Leplay, Fracture and cohesive parameter identification of refractories by Digital Image Correlation up to 1200 °C, *Experimental Mechanics* (2020).
- [22] R. Vargas, R. B. Canto, F. Hild, Fracture energy evaluation of refractories in wedge splitting tests from notch opening displacements, *Journal of the European Ceramic Society* 41 (10) (2021) 5367–5379. doi:10.1016/j.jeurceramsoc.2021.02.055.
- [23] A. Hillerborg, M. Modeer, P. Petersson, Analysis of crack formation and crack growth in concrete by means of fracture mechanics and finite elements, *Cement Conc. Res.* 6 (1976) 773–782.
- [24] E. Tschegg, Prüfeinrichtung zur Ermittlung von bruchmechanischen Kennwerten sowie hierfür geeignete, Prüfkörper, Austrian Pat. AT 390328B, registered (1986).
- [25] E. Brühwiler, F. H. Wittmann, The wedge splitting test, a new method of performing stable fracture mechanics tests, *Engineering Fracture Mechanics* 35 (1-3) (1990) 117–125.
- [26] R. Vargas, X. Pinelli, B. Smaniotto, F. Hild, R. B. Canto, Effect of sintering temperature on fracture energy of Alumina-Mullite-Zirconia castable at 600°C, *Journal of the European Ceramic Society* 41 (7) (2021) 4406–4418.
- [27] K. Kavanagh, R. Clough, Finite element applications in the characterization of elastic solids, *Int. J. Solids Struct.* 7 (1971) 11–23.
- [28] K. Kavanagh, Extension of classical experimental techniques for characterizing composite-material behavior, *Exp. Mech.* 12 (1) (1972) 50–56.
- [29] E. Pagnacco, A.-S. Caro-Bretelle, P. Jenny, *Parameter Identification from Mechanical Field Measurements using Finite Element Model Updating Strategies*, Wiley-Blackwell, 2012, Ch. 9, pp. 247–274.
- [30] S. Roux, F. Hild, Optimal procedure for the identification of constitutive parameters from experimentally measured displacement fields, *Inter-*

- national Journal of Solids and Structures 184 (2020) 14–23.
- [31] K. Park, G. H. Paulino, J. R. Roesler, A unified potential-based cohesive model of mixed-mode fracture, *Journal of the Mechanics and Physics of Solids* 57 (6) (2009) 891–908.
- [32] K. Park, G. H. Paulino, Computational implementation of the PPR potential-based cohesive model in ABAQUS: educational perspective, *Engineering Fracture Mechanics* 93 (2012) 239–262.
- [33] J.-S. Affagard, F. Mathieu, J.-M. Guimard, F. Hild, Identification method for the mixed mode interlaminar behavior of a thermoset composite using displacement field measurements and load data, *Composites Part A: Applied Science and Manufacturing* 91 (2016) 238–249.
- [34] M. D. Cabrelon, A. H. A. Pereira, J. Medeiros, R. D. Toledo-Filho, J. A. Rodrigues, Efeito do tempo de exposição a uma atmosfera coqueificante na microestrutura e nas propriedades de um concreto refratário usado na indústria petroquímica, *Cerâmica* 58 (2012) 195–204.
- [35] D. Y. Miyaji, C. Z. Otofujii, M. D. Cabrelon, J. Medeiros, J. A. de Rodrigues, The coke effect on the fracture energy of a refractory castable for the petrochemical industry, in: *Proceedings of the Unified International Technical Conference on Refractories (UNITECR 2013)*, John Wiley & Sons, Inc., 2014, pp. 1111–1116. doi:10.1002/9781118837009.ch188.
URL <http://dx.doi.org/10.1002/9781118837009.ch188>
- [36] A. H. A. Pereira, D. Y. Miyaji, M. D. Cabrelon, J. Medeiros, J. A. Rodrigues, A study about the contribution of the α - β phase transition of quartz to thermal cycle damage of a refractory used in fluidized catalytic cracking units, *Cerâmica* 60 (2014) 449–456.
- [37] A. Tarantola, *Inverse Problems Theory. Methods for Data Fitting and Model Parameter Estimation*, Elsevier Applied Science, Southampton (UK), 1987.
- [38] A. Carpiuc-Prisacari, M. Poncelet, K. Kazymyrenko, F. Hild, H. Leclerc, Comparison between experimental and numerical results of mixed-mode crack propagation in concrete: Influence of boundary conditions choice, *Cement and Concrete Research* 100 (2017) 329–340.
- [39] R. Vargas, A. Tsitova, F. Bernachy-Barbe, B. Bary, R. Canto, F. Hild, On the identification and validation of fracture mechanics models for curved crack in mortar, *Strain* 56 (6) (2020) e12364.